AGU PUBLICATIONS

JGR

Journal of Geophysical Research: Oceans

RESEARCH ARTICLE

10.1002/2013JC009262

Key Points:
- The density-driven current in Jiaozhou Bay was simulated by a diagnostic model
- The results by nonsynchronous data are quite different with synchronous data
- The results by tidally averaged data are consistent with synchronous data

Correspondence to:
Z. Liu,
zliu@ouc.edu.cn

Citation:
Cai, Z., Z. Liu, X. Guo, H. Gao, and Q. Wang (2014), Influences of intratidal variations in density field on the subtidal currents: Implication from a synchronized observation by multiships and a diagnostic calculation, *J. Geophys. Res. Oceans*, *119*, 2017–2033, doi:10.1002/2013JC009262.

Received 9 JULY 2013
Accepted 10 FEB 2014
Accepted article online 18 FEB 2014
Published online 18 MAR 2014

Influences of intratidal variations in density field on the subtidal currents: Implication from a synchronized observation by multiships and a diagnostic calculation

Zhongya Cai[1], Zhe Liu[1], Xinyu Guo[2], Huiwang Gao[1], and Qiang Wang[3]

[1]Key Laboratory of Marine Environment and Ecology, Ministry of Education, Ocean University of China, Qingdao, China, [2]Center for Marine Environmental Studies, Ehime University, Matsuyama, Japan, [3]North China Sea Marine Forecasting Center of State Oceanic Administration, Qingdao, China

Abstract Using synchronous observational water temperature and salinity data collected simultaneously by 21 ships in summer and a three-dimensional robust diagnostic model, we calculated the density-driven current in Jiaozhou Bay (JZB), a semienclosed bay in the Yellow Sea. Special attention was paid to the influences of intratidal variations in temperature and salinity on the density-driven current. The density-driven current in JZB has a maximum speed of $\sim$0.1 m s^{-1} and is stronger than the tide-induced residual current in some places. The density-driven current is characterized by the intrusion of high-density (low-density) water in deep (shallow) areas. The results of the diagnostic model depend heavily on the observational data. For example, the density-driven current calculated from nonsynchronous data obtained by one ship at the same 21 stations is not consistent with that calculated from synchronous data because the nonsynchronous data correspond to different tidal phases at different stations. The intratidal variations of the density field result in a false spatial variation of density in the nonsynchronous data, which induces a false density-driven current that is of the same order as that calculated from the synchronous data. In contrast, the tidally averaged water temperature and salinity, which were used to remove intratidal variations from the synchronous data, diagnosed a density-driven current consistent with that from synchronous data. We, therefore, conclude that it is not necessary to explicitly resolve the intratidal variations in density in the calculation of density-driven current, but it is necessary to remove intratidal variations in the density field before the calculation.

1. Introduction

Density-driven current, an important component of coastal circulation, can be calculated by diagnostic models [*Sarkisyan and Ivanov*, 1971; *Holland and Hirschman*, 1972]. It is commonly known that the accuracy of a diagnostic model depends on the quality of water temperature and salinity data used [*Holland and Hirschman*, 1972]. In the open ocean, the hydrographic properties of water vary slowly; thus, steady fields of water temperature and salinity are usually used in diagnostic models [*Sarkisyan and Ivanov*, 1971; *Holland and Hirschman*, 1972; *Sarmiento and Bryan*, 1982; *Fujio and Imasato*, 1991]. However, the strong tidal current in coastal regions and consequent intratidal variations in water temperature and salinity suggest that it is not reasonable to diagnose the density-driven current in a semienclosed bay using steady fields of water temperature and salinity.

In principle, the intratidal variations in water temperature and salinity require the use of synchronous in situ observation data with sufficient temporal and spatial resolutions to diagnose a density-driven current. However, it is very difficult to obtain the labor, equipment, and financial resources required to engage dozens of survey ships simultaneously to make synchronous observations. In practice, nonsynchronous data (e.g., data collected at different stations at different times by one ship) or so-called climatological mean data (i.e., the statistical means of data measured on several cruises over many years) are most widely used in diagnostic models, and the impact of intratidal variations of temperature and salinity on density-driven currents has seldom been reported [e.g., *Fujio and Imasato*, 1991; *Yanagi and Takahashi*, 1993; *Guo and Yanagi*, 1996; *Guo et al*., 2004; *Lee et al*., 2004; *Lee and Chao*, 2003; *Liu et al*., 2010].

In the summer of 2009, we used 21 ships to carry out a synchronous observation at 21 stations in a semienclosed bay, Jiaozhou Bay (JZB), on the western coast of the Yellow Sea. Using the synchronously observed

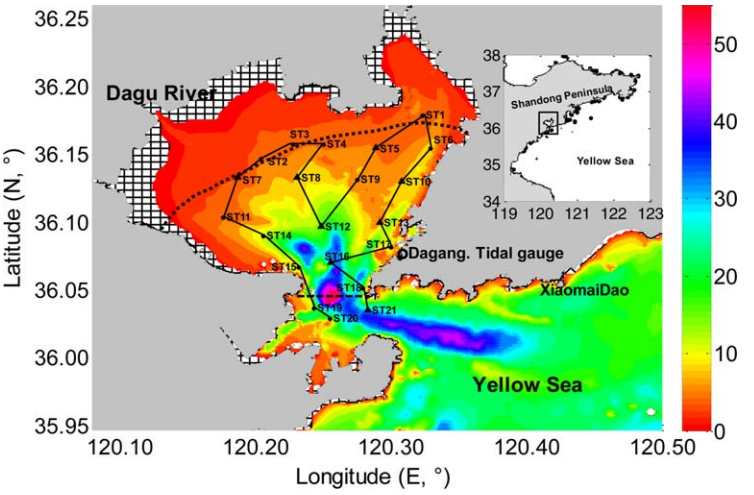

Figure 1. Bathymetry (m) of Jiaozhou Bay. The inset in the top-right corner shows the location of Jiaozhou Bay. The gridded region is the tidal flat. "ST" followed by a number denotes the sampling stations where observations were conducted in August 2009. Additional surface current data were collected at stations denoted by black triangles. The winds and sea level were recorded at Xiaomaidao and Dagang, respectively. The black line is the route of the virtual observation described in section 2.1. The black dashed line denotes the section across which the density-driven current is shown in Figure 8, and the dotted line at bay head denotes the location of the cross-sea bridge's piers in JZB.

water temperature and salinity data from this field campaign, we established a three-dimensional robust diagnostic model to demonstrate how and to what extent the intratidal variations in the water temperature and salinity affect the density-driven current.

JZB (35°58′N–-36°18′N, 120°04′E–120°23′E) is a semi-enclosed shallow water body with an area of ~397 km^2, an average depth of approximately 7 m, and a maximum depth of ~60 m at the bay mouth (Figure 1). JZB is connected to the Yellow Sea by a narrow channel. Freshwater input into the bay comes primarily from the Dagu River (Figure 1) [*Han et al*., 2007]. The water movement in JZB is affected by strong tidal currents, of which the M_2 tidal constituent is the strongest [*Ding*, 1992]. Under the influence of semidiurnal tides, the water temperature and salinity have been reported to vary intratidally [*Liu et al*., 2005]. However, the density-driven current in JZB and the influences of intratidal variations in water temperature and salinity on this current have not been reported in previous studies [e.g., *Shi et al*., 2011; *Wang et al*., 2009; *Liu et al*., 2007, 2004; *Chen et al*., 1999].

2. Data and Methods

2.1. Field Observations and Data Processing

To reveal the spatial and intratidal variations of water temperature and salinity in JZB, a synchronous observation campaign was conducted in August 2009. The observation network comprised 21 anchor stations (Figure 1). At each anchor station, one boat with three to four persons and one set of conductivity-temperature-depth (CTD) (see Table 1 for the type of instrument) were used. In total, 21 ships and >80 crewmembers worked together. The observation began at approximately 13:00 on 17 August and lasted over 25 h (i.e., one lunar day). However, it began to rain at 06:00 on 18 August. To exclude the effects of the rain, we used only the in situ observational data of temperature and salinity in the first M_2 tidal period in this study. In addition to the in situ data, the hourly winds measured at the Xiaomaidao weather station and sea level data from 1 August 2009 to 31 August 2009 recorded at Dagang tidal gauge were also used in this study. The temperature, salinity, and wind data were used to drive the model, and the current and sea level data were used to validate the model results.

Generally, vertical profiles of water temperature and salinity were obtained each hour at each station, except for at some shallow stations (Table 1). At these shallow stations, we measured water temperature and salinity only in the surface layer (1.0–1.5 m). As we prepared the data for the diagnostic model, we assumed vertical homogeneity at these shallow stations. The interpolation of in situ data to the model grid was conducted linearly in the vertical direction at each station and trigonometrically in the horizontal direction. Linear interpolation was applied to obtain data at each time step throughout the calculation. In addition to the hydrographic data taken at all 21 stations, the surface current was also measured at eight stations (black triangles in Figure 1) by current meters (Table 1). These current data as well as the sea level data at Dagang tidal station (Figure 1) were used to validate the model results.

Table 1. Position and Mean Depth of the Observation Stations, Sampling Depth at Each Station, Instruments and Sampling Interval for Water Temperature (T) and Salinity (S), Observation Time at Each Station by the Virtual Ship Described in Section 2.1 and Corresponding Tidal Phase at the Virtual Ship's Observation Time

Station	Location	Mean Depth (m)	Sampling Layer (m)	Instrument[a]		Sampling Interval		Time	Tide Phase
				S	T	S	T		
ST1	120.325E, 36.179N	4.0	~1.0	SYA2-2	RBR TDR-2050	1 h	1 min	17 Aug 18:34:02	Max ebb-low tide
ST2	120.205E, 36.147N	2.6	Profile	Alec AAQ1183		1 h		17 Aug 22:10:19	Low tide-max flood
ST3	120.226E, 36.158N	3.6	~1.0	SYA2-2	RBR TDR-2050	1 h	1 min	17 Aug 21:43:13	Low tide-max flood
ST4	120.250E, 36.158N	4.0	~1.0	RBR XR-420-CTD		1 min		17 Aug 21:16:07	Low tide (21:00)
ST5	120.289E, 36.155N	5.0	~1.0	SYA2-2	RBR TDR-2050	1 h	1 min	17 Aug 19:07:25	Max ebb-low tide
ST6	120.330E, 36.155N	8.0	Profile	RBR XR-420-CTD		1 h		17 Aug 18:05:20	Max ebb-low tide
ST7	120.187E, 36.133N	6.0	~1.0	SYA2-2	RBR TDR-2050	1 h	1 min	17 Aug 22:37:36	Low tide-max flood
ST8	120.231E, 36.133N	7.0	Profile	Alec AAQ1183		1 h		17 Aug 20:45:25	Low tide (21:00)
ST9	120.276E, 36.132N	6.0	~1.5	RBR XR-420-CTD		1 min		17 Aug 19:36:47	Max ebb-low tide
ST10	120.308E, 36.130N	6.0	~1.5	RBR XR-420-CTD		1 min		17 Aug 17:34:20	Max ebb-low tide
ST11	120.177E, 36.104N	3.9	~1.0	SYA2-2	RBR TDR-2050	1 h	1 min	17 Aug 23:08:22	Low tide-max flood
ST12	120.249E, 36.097N	15.0	Profile	RBR XR-620		1 h		17 Aug 20:11:28	Max ebb-low tide
ST13	120.292E, 36.100N	3.9	~1.0	Alec Compact-CT	Alec Compact-TD	1 min		17 Aug 17:02:33	Max ebb (17:00)
ST14	120.207E, 36.090N	11.2	Profile	Alec Compact-CT	Alec Compact-TD	1 h		17 Aug 23:38:35	Max flood (00:00)
ST15	120.233E, 36.067N	9.6	Profile	Alec Compact-CT	Alec Compact-TD	1 h		18 Aug 00:09:47	Max flood (00:00)
ST16	120.254E, 36.070N	21.5	Profile	RBR XR-620		1 h		17 Aug 16:01:04	High tide-max ebb
ST17	120.301E, 36.082N	8.8	Profile	Alec Compact-CT	Alec Compact-TD	1 h		17 Aug 16:35:34	Max ebb (17:00)
ST18	120.280E, 36.052N	16.4	Profile	Alec Compact CTD		1 h		17 Aug 15:27:02	High tide-max ebb
ST19	120.244E, 36.037N	5.6	~1.0	SYA2-2	Alec Compact-TD	1 h	1 min	18 Aug 00:41:08	Max flood-high tide
ST20	120.256E, 36.029N	12.0	Profile	Alec Compact-CT	Alec Compact-TD	1 h		18 Aug 01:07:16	Max flood-high tide
ST21	120.283E, 36.035N	28.3	Profile	RBR XR-620		1 h		17 Aug 15:00:00	High tide (14:00)

[a]SYA2-2 is a salinity meter made by Tianjin Marine Environmental Monitoring Central Station. TDR-2050 is a temperature and depth logger produced by RBR Ltd. AAQ1183 is a modernized compact and light-weight multiparameter water quality meter produced by Alec Electronics Co., Ltd. RBR XR-420-CTD and XR-620 are conductivity, temperature, and depth loggers produced by RBR Ltd. Compact-TD, Compact-CT, and Compact-CTD are small, highly accurate two-channel recorders for temperature-depth, conductivity-temperature, and conductivity-temperature-depth, respectively, produced by Alec Electronics Co., Ltd.

To determine the difference between synchronous data and nonsynchronous data, we designed a virtual observation to obtain nonsynchronous data from the hourly measured synchronous data. To simulate typical nonsynchronous observations, we assumed that only one ship with a speed of 10 nautical miles per hour visited all the stations and spent 20 min sampling at each station. With these assumptions, the virtual observation started at 15:00 on 17 August at station ST21 and finished approximately 10 h later at station ST20. The ship's route is shown in Figure 1. The data for the virtual survey were derived from the data from the synchronous observation at the arrival time of the virtual ship at each station. If the arrival time of the virtual ship did not coincide exactly with the real sampling time at that station, a linear interpolation in time was applied to the two neighboring data points to calculate the data for the virtual observation. The tidally averaged fields of water temperature and salinity were obtained by temporally averaging the hourly synchronous data. The nonsynchronous data and the tidally averaged data were spatially interpolated to all the grid points and fixed throughout the calculation.

2.2. Robust Diagnostic Model

Sarmiento and Bryan [1982] proposed the concept of robust diagnostic model, which has since been widely used by many studies to calculate density-related currents [*Fujio and Imasato*, 1991; *Yanagi and Takahashi*, 1993; *Guo and Yanagi*, 1996; *Guo et al*., 2004; *Lee et al*., 2004; *Lee and Chao*, 2003; *Wright et al*., 2006; *Liu et al*., 2010].

Based on the Princeton Ocean Model [*Blumberg and Mellor*, 1987; *Mellor*, 2004], we established a robust diagnostic model following the method of *Sarmiento and Bryan* [1982]. The original Princeton Ocean Model was modified by adding a damping term to the right-hand side of the conservation equations for water temperature and salinity:

$$\frac{\partial C}{\partial t}+\frac{\partial uC}{\partial x}+\frac{\partial vC}{\partial y}+\frac{1}{D}\frac{\partial \omega C}{\partial \sigma}=\frac{\partial}{\partial x}\left(A_H\frac{\partial C}{\partial x}\right)+\frac{\partial}{\partial y}\left(A_H\frac{\partial C}{\partial y}\right)+\frac{1}{D}\frac{\partial}{\partial \sigma}\left(\frac{A_v}{D}\frac{\partial C}{\partial \sigma}\right)+\gamma(C^*-C), \quad (1)$$

where C represents the water temperature or salinity; t is the time; x, y, and σ are the three spatial coordinates; u, v, and ω are the components of the velocity in the three respective spatial coordinates; A_H and A_v are the horizontal and vertical diffusivity coefficients, respectively; C^* is the datum observed at each grid point interpolated from the in situ observational data; and γ is a nonnegative constant controlling the role

of the observed data C^*. The last term in equation (1) prevents the calculated value C from deviating greatly from the observed value C^*.

The model domain (Figure 1) includes a tidal flat region, which was treated by a wetting and drying scheme [*Oey*, 2005]. There are 159 × 185 grid points with a resolution of 200 m in the horizontal direction and 15 evenly arranged vertical levels. The time step is 1.5 s for the external mode and 12 s for the internal mode. In addition to prescribing the observational data for C^* in equation (1), we also specified the M_2 and S_2 tidal forcings at the open boundary and wind stresses at the sea surface. The amplitudes and phases of the M_2 and S_2 tidal constituents at the open boundary were obtained from the marine atlas of the Bohai Sea, Yellow Sea, and East China Sea [*Chen et al.*, 1992]. The radiation condition was used for the normal component of the velocity and no-flux condition was used for salinity and temperature along the open boundary. The wind stress (τ) was calculated from the wind data collected at the Xiaomaidao weather station (Figure 1) as follows:

$$\tau = \rho_a C_D U_{10}^2, \tag{2}$$

where $\rho_a = 1.3$ kg m^{-3} is the density of air, U_{10} is the wind speed (m s^{-1}) at 10 m and C_D is the drag coefficient, which has a value of 1.64×10^{-3}, according to the equation given by *Stewart* [2008]. The current and sea level were initialized to zero and the calculation time was 70 days.

Synchronous data were used in Case 1 (Table 2), which includes the influence of intratidal variations in water temperature and salinity on the density-driven current. Nonsynchronous data collected by the virtual ship were used in Case 2 (Table 2), which calculates a false density-driven current caused by false spatial variations in the density field arising from temporal (intratidal) variations in water temperature and salinity. Tidally averaged data were used in Case 3 (Table 2), which clarifies the strength of the influences of intratidal variations in water temperature and salinity on the density-driven current.

The hourly model results of these three cases on the last 25 h were saved for further analysis after they reached equilibrium. The density-driven current in these cases was obtained by subtracting the overall current from an accompanying calculation of current in which the tide and surface winds were considered but a constant density was used. This subtraction method was applied to the model results saved on the last 25 h in the three cases. The difference in the hourly current field given by the subtraction method on the last 25 h was averaged to obtain the tidally averaged density-driven current.

In the robust diagnostic model, an important issue is the determination of the damping coefficient γ. If γ is zero, the modeled temperature and salinity are independent of the observation data and the model is a fully prognostic model. As γ becomes larger, C^* plays a more important role. As γ tends toward infinity, the model becomes a purely diagnostic model ($C = C^*$).

To examine the relative importance of the damping term to the horizontal advection term in equation (1), *Sarmiento and Bryan* [1982] introduced a scale velocity V^* and a scale length L^* so that the ratio of the damping term to the horizontal advection term is $\gamma L^*/V^*$. The authors calculated the circulation in the Atlantic using a depth-dependent γ that decreased from 1/50 day^{-1} at the surface to 1/250 day^{-1} at the bottom. Because the scale length L^* is much smaller in JZB than in the Atlantic, a larger γ is needed to make the damping term balance the advection term. In addition, because the data in this study were measured synchronously, a large γ is preferred because high-quality data help to diagnose a reliable flow field.

Because the density-driven current is primarily driven by the baroclinic pressure gradient, we need to know how the horizontal gradient of density in the model changes with the damping coefficient γ. A variable M, representing the magnitude of the horizontal gradient in the density field, is defined as

Table 2. Conditions Used in the Numerical Experiments to Investigate the Mechanisms Governing the Density-Driven Current

Case	Type of Data	Vertical Turbulent Viscosity Coefficient	Usage
1	Hourly synchronous data	Calculated in the model	Background flow field
2	Nonsynchronous data	Calculated in the model	Effects of nonsynchronous data on density-driven current
3	Tidally averaged data	Calculated in the model	Effects of tidally averaged data on density-driven current
4	Hourly synchronous data	From Case 2	Effects of vertical turbulent viscosity in Case 2 on density-driven current
5	Hourly synchronous data	From Case 3	Effects of vertical turbulent viscosity in Case 3 on density-driven current

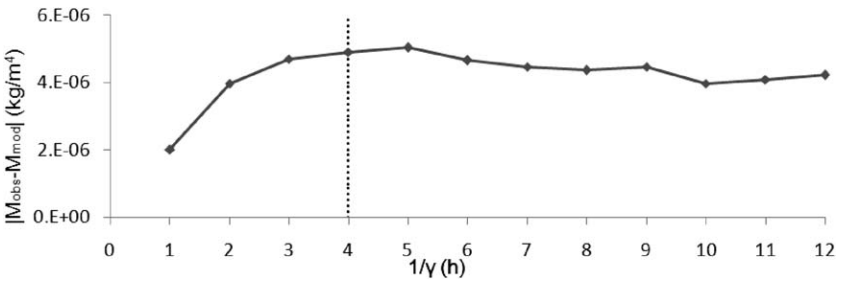

Figure 2. Absolute difference in the averaged horizontal gradient of the modeled water density (M_{model}) and the observed water density (M_{obs}) versus the damping coefficient γ. See equation (1) for the definition of γ and equation (3) for the definition of M.

$$M=\sqrt{\left(\frac{\partial\rho}{\partial x}+\frac{\partial\rho}{\partial\sigma}\frac{\partial\sigma}{\partial x}\right)^2+\left(\frac{\partial\rho}{\partial y}+\frac{\partial\rho}{\partial\sigma}\frac{\partial\sigma}{\partial y}\right)^2}, \tag{3}$$

where ρ is the density. Figure 2 shows the spatial mean of the difference in M between observation and simulation in JZB as a function of γ^{-1}. As γ decreases, the difference between the objectively interpolated water temperature and salinity and those calculated by equation (1) increase and the density distribution is gradually controlled more by the advection term in equation (1). The difference between the modeled and observed density gradient becomes relatively stable when γ is lower than 0.25 h^{-1} (Figure 2), indicating that the density distribution is approximately stable after being adjusted by equation (1). Hence, γ was set to a slightly higher value (0.25 h^{-1}) to retain the information of the synchronous observation data as much as possible in this study.

3. Results

3.1. Model Validation

The model was calibrated with the sea level at Dagang tidal station and the sea surface current measured at eight stations (Figure 1). The error in the M_2 amplitude and the phase of sea level between observation and simulation are 0.02 m and 0.54°, respectively. Because the velocity data were measured only over a 25 h period, the ellipse parameters of the semidiurnal tide were used to validate the calculation of velocity. At ST12 and ST16, the results differ a little largely from the observation (Table 3). A reasonable explanation on this conflict is the resolution of the model (i.e., 200 m) that is apparently insufficient to resolve the steep topography around two stations (Figure 1). But at most stations the simulated and observed harmonic constants of tidal currents show reasonable agreement (Table 3). The mean difference of the semimajor axis between the simulated and observed velocities is 0.11 m s^{-1}. The mean difference of ellipse inclination and phase is both $<15°$.

Because this study focuses on the density-driven current, it is also necessary to validate the subtidal currents in the model output. The overall subtidal current, which was calculated by averaging the observed current velocity over the 25 h period, has three components: the tide-induced residual current, the density-driven current, and the wind-driven current. It is difficult to separate these three components of the observation. Therefore, to validate the model result, tidal, and wind forcing as well as the temperature and salinity fields were all included in the model calculation. The modeled subtidal current in Case 1 was then obtained by averaging the model results over the 25 h period.

According to Table 4, the magnitude of the subtidal current is usually one order of magnitude smaller than that of tidal current in JZB. Consequently, it is more difficult to accurately simulate the subtidal current than the tidal current. Besides, the existence of the cross-sea bridge (Figure 1) can affect the subtidal current by altering local topography. The diameter of the bridge piers is 1.8 m and the distance between ST7 and its nearest pier is <200 m. Owing to the horizontal resolution of 200 m, it is difficult for the model to take into account the influence of cross-sea bridge on the currents and consequently we observed a slightly large error between simulated current and observation data at ST7. However, the modeled subtidal currents are generally consistent with the observed currents at most stations. The differences in direction and magnitude

Table 3. Observed and Modeled Tidal Ellipse Parameters for Surface Semidiurnal Tides at the Stations in Figure 1

	Observation				Simulation				Absolute Value of Difference Between Observation and Simulation			
Station	Semimajor Axis (m s^{-1})	Semiminor Axis (m s^{-1})	Inclination (°)	Phase (°)	Semimajor Axis (m s^{-1})	Semiminor Axis (m s^{-1})	Inclination (°)	Phase (°)	Semimajor Axis (m s^{-1})	Semiminor Axis (m s^{-1})	Inclination (°)	Phase (°)
ST5	0.36	0.08	43.93	59.35	0.28	0.03	59.13	46.32	0.08	0.05	15.2	13.03
ST7	0.30	0	110.51	45.13	0.33	0.01	126.81	45.59	0.03	0.01	16.3	0.46
ST8	0.31	0.04	97.06	65.2	0.31	0.04	101.25	51.72	0.00	0	4.19	13.48
ST10	0.30	0.02	54.14	30.07	0.33	0.03	62.92	47.06	0.03	0.01	8.78	16.99
ST12	0.24	0.01	128.91	15.49	0.36	0	98.77	56.38	0.12	0.01	30.14	40.89
ST13	0.29	0.05	59.74	24.5	0.37	0.07	65.51	34.17	0.08	0.02	5.77	9.67
ST16	1.09	0.01	97.24	65.39	0.64	0.05	100.74	62.84	0.45	0.04	3.5	2.55
ST21	0.8	0.03	154.58	54.9	0.88	0.06	153.2	38.85	0.08	0.03	1.38	16.05
Mean									0.11	0.02	10.66	14.14
RMS									0.14	0.02	9.55	12.37

of the modeled and observed subtidal currents are approximately 35° and 30%, respectively. We, therefore, conclude that the diagnostic model can capture the general features of the residual current in JZB.

3.2. Modeled Temperature and Salinity Fields

Figure 3 shows the horizontal distributions of the calculated temperature, salinity, and density during the M_2 tidal cycle. The hydrographic features in JZB are influenced by the freshwater input from rivers and the intrusion of Yellow Sea water from the bay mouth. The former is characterized by low salinity and low density, whereas the latter has high salinity and high density. In addition, the combination of surface heating, tidal mixing, and bathymetry results in high temperatures in shallow regions (e.g., at the bay head) and low temperatures in deep regions (e.g., at the bay mouth). Fronts of salinity and density are found in the offshore area near the Dagu River mouth. The position of the fronts changes within a tidal cycle. During the flood tide, the fronts move to the river mouth as the low-temperature, high-salinity Yellow Sea water enters the bay. During the ebb tide, the fronts move to the bay mouth as the Yellow Sea water exits (Figure 3).

The spatial variations in water temperature, salinity, and density over the entire bay are ~2.5°C, 1.50, and 2.0 kg m^{-3}, respectively, as observed in their tidally averaged fields (Figure 4, top). The temporal variation is demonstrated by the difference between the maximum and minimum values of temperature, salinity, and density in a tidal cycle (Figure 4, bottom). The range of the temporal variations in water temperature, salinity, and density is ~1.5°C, 1.50, and 1.5 kg m^{-3}, respectively, near the river mouths; these ranges decrease toward the bay mouth.

3.3. The Density-Driven Current Calculated With Synchronous Data

In the surface layer (Figure 5a), the density-driven current is southward around the bay mouth, flowing from the shallow area to the deep area. The current is westward in the northern area of the bay and southwestward in the western area of the bay (Figure 5a). The maximum speed of the surface density-driven current is >0.1 m s^{-1} near the bay mouth. In the bottom layer (Figure 5b), the density-driven current is generally weak and in a different direction than that in the surface layer. At the bay mouth, the bottom

Table 4. The Comparison of Residual Currents From Observation and From the Diagnostic Model in the Surface Layer[a]

	Observation		Simulation			
Station	Magnitude (cm s^{-1})	Direction (°)	Magnitude (cm s^{-1})	Direction (°)	Relative Difference of Magnitude (%)	Absolute Difference of Direction (°)
ST5	2.1	−65.8	1.7	−91.6	17.3	25.8
ST7	1.6	49.7	0.8	−85.3	51.8	135.0
ST8	5.2	205.9	5.0	209.4	3.2	−3.5
ST10	4.1	−65.0	3.4	−141.0	15.7	76.0
ST12	5.2	−60.1	6.3	−78.6	20.8	18.5
ST13	3.0	151.0	3.7	173.8	25.1	−22.8
ST16	25.1	52.4	14.3	32.9	43.2	19.5
ST21	23.3	237.1	18.6	206.5	20.2	30.6

[a]The angles 0°, 90°, 180°, and 270° indicate that the direction of flow is north, east, south, and west, respectively.

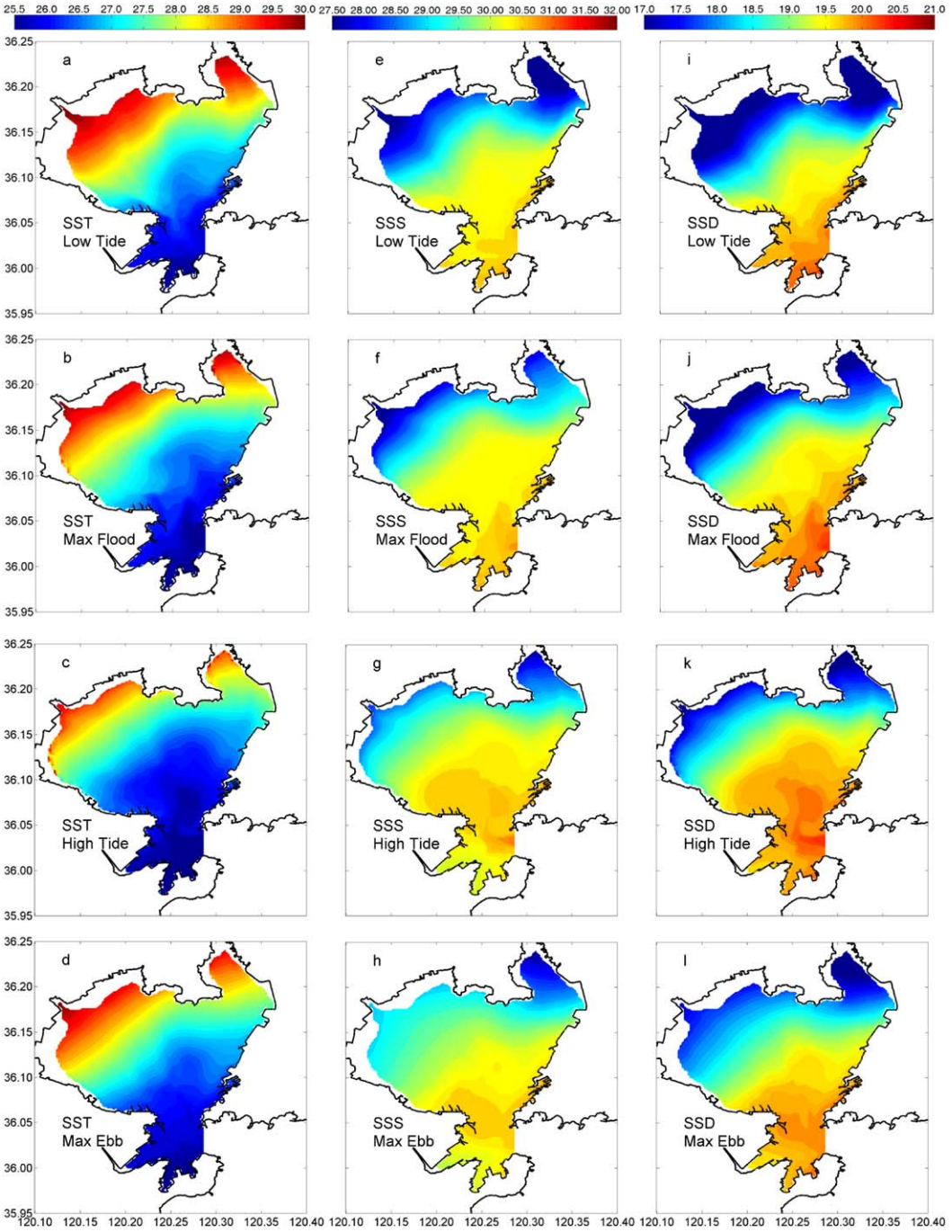

Figure 3. (left) Sea surface temperature (°C), (middle) sea surface salinity, and (right) sea surface density (σ_t) obtained by synchronous observation at different tidal phases (low tide, maximum flood, high tide, and maximum ebb).

density-driven current is northward, flowing into the bay through the deep western channel (see Figure 1 for bathymetry).

The vertical distribution of the density-driven current normal to a section across the bay mouth is presented in Figure 6. The current is southward in the upper layer but northward in the lower layer. The interface of the two opposite currents is at a depth of ~20 m. It is clear that the Yellow Sea water enters JZB in the bottom layer while the bay water leaves JZB in the surface layer.

The water movement in JZB is dominated by tidal motion and M_2 tide is the dominant tidal constituent that accounts for 80% of kinetic energy [*Ding*, 1992]. The magnitude of tidal currents is higher than that of

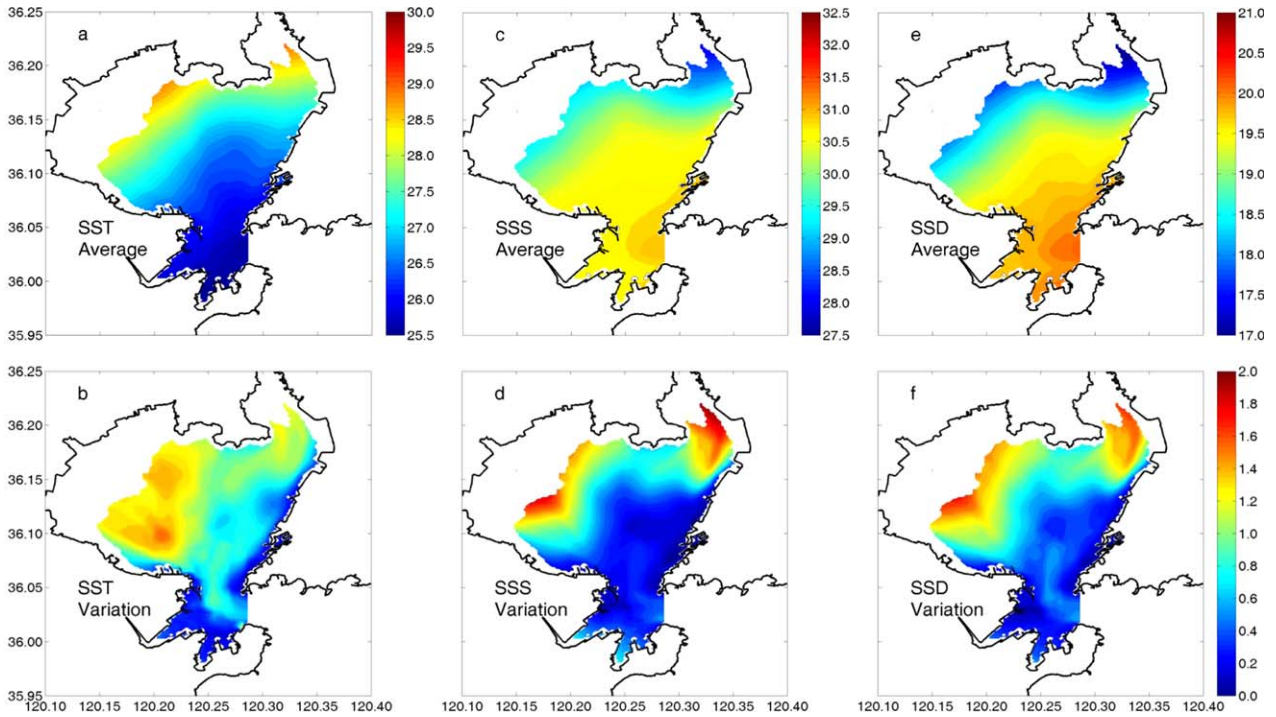

Figure 4. (a) Tidally averaged sea surface temperature (°C), (c) sea surface salinity, and (e) sea surface density (σ_t) and (b) difference between the maximum and minimum values of sea surface temperature (°C), (d) sea surface salinity, and (f) sea surface density (σ_t) over a tidal cycle.

subtidal currents by one order. Owing to the nonlinear effects in the tidal currents, tide-induced residual current inevitably accompanies the tidal currents throughout the year. Following many previous studies [e.g., *Shi et al*., 2011; *Chen et al*., 2011; *Lv et al*., 2010; *Lou et al*., 2009; *Liu et al*., 2004], tidal motion is considered to provide a background for the physical variables such as water temperature, salinity, and density-driven currents in this study. The tide-induced residual current in the surface layer is strong around the bay mouth, where its magnitude is larger than 0.1 m s^{-1} (Figure 7a). It is weaker in the central part and bay head. Generally, the tide-induced residual current is weaker in the bottom layer (Figure 7c) than in the surface layer (Figure 7a). The spatial pattern of the tide-induced residual current found in this study (Figures 7a and 7c) is consistent with that reported in previous studies [e.g., *Lou et al*., 2009; *Shi et al*., 2011].

The magnitude ratio α of the density-driven current to the tide-induced residual current was calculated as follows:

$$\alpha = |\vec{V}_d| / |\vec{V}_t|, \tag{4}$$

where $\vec{V}_d$ is the density-driven current and $\vec{V}_t$ is the tide-induced residual current. The ratio in the surface (bottom) layer was calculated for areas where the magnitude of $\vec{V}_t$ is greater than 0.01 m s^{-1} (0.005 m s^{-1}). The ratio is greater than 0.5 in most areas of both the surface and bottom layers (Figures 7b and 7d), indicating that the density-driven current is an important component in the summer circulation in JZB.

3.4. The Density-Driven Current Calculated With Nonsynchronous Data

As described in section 2.1, nonsynchronous data were obtained by "implementing" a virtual observation. The density field from nonsynchronous data generally has the same spatial distribution as the averaged synchronous density field. We can identify the low-density area in the northwestern area of JZB in both the surface and bottom layers (Figures 8a and 8c). However, the difference between the nonsynchronous data and averaged synchronous data (Figures 8b and 8d) is also clear. For example, the water density in western part of JZB is lower in the nonsynchronous data than in the tidally averaged synchronous data (e.g., the difference of about ~2.0 kg m^{-3} off Dagu River mouth), while the density in eastern part of JZB is higher in the nonsynchronous data than in the tidally averaged synchronous data (e.g., the difference of about ~0.3

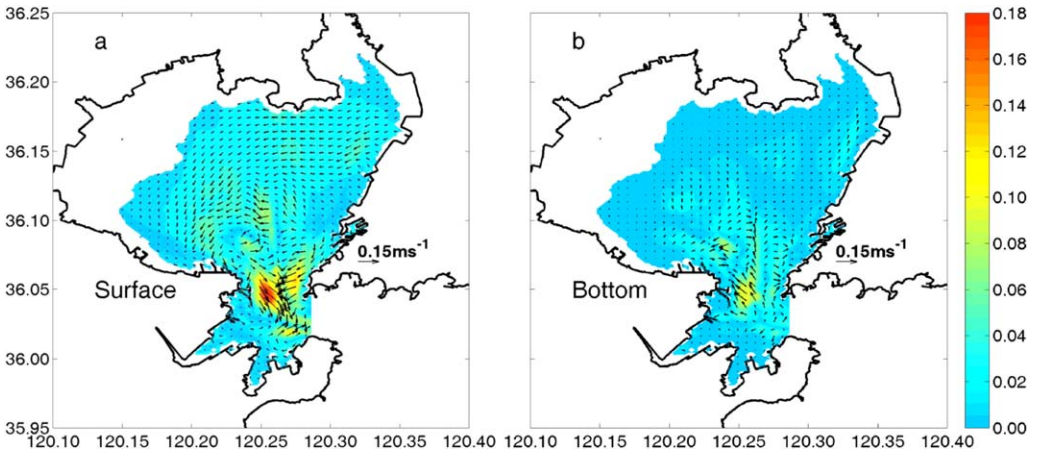

Figure 5. Horizontal distribution of the tidally averaged density-driven current (m s^{-1}) in the (a) surface layer (the topmost sigma layer) and (b) bottom layer (the lowest sigma layer). The color shows the magnitude of the velocity. This definition of the surface and bottom layers is also used in the following figures.

kg m^{-3} in the northeast of JZB) (Figures 8b and 8d). Consequently, the horizontal spatial gradient in density is greater in the nonsynchronous data than in the tidally averaged synchronous data.

In Case 2, the density-driven current calculated using the nonsynchronous data (Figures 9a and 9c) is stronger than that calculated using the synchronous data (Figure 5). For example, the density-driven current in the surface layer is intensified offshore of the Dagu River mouth, where the density gradient is greater in the nonsynchronous data than in the synchronous data (Figure 8). The direction of the density-driven current also changes. For example, the surface density-driven current north of the bay mouth becomes eastward (Figure 9a). In the bottom layer, a strong northward inflow is found offshore of the Dagu River mouth and an apparent westward current is found north of the bay mouth (Figure 9c). These features are significantly different from those found using the synchronous data (Figure 5).

The vector difference (β_1) and relative difference (β_2) between the density-driven current calculated with the nonsynchronous and synchronous data in the surface (Figure 9b) and bottom (Figure 9d) layers were calculated as follows:

$$\begin{aligned} \beta_1 &= \vec{V}_s - \vec{V}_{ns} \\ \beta_2 &= ||\vec{V}_s| - |\vec{V}_{ns}||/|\vec{V}_s|, \end{aligned} \tag{5}$$

where $\vec{V}_s$ is the velocity calculated with the synchronous data (Case 1) and $\vec{V}_{ns}$ is that calculated with the nonsynchronous data (Case 2). In areas where the density-driven current calculated with the synchronous

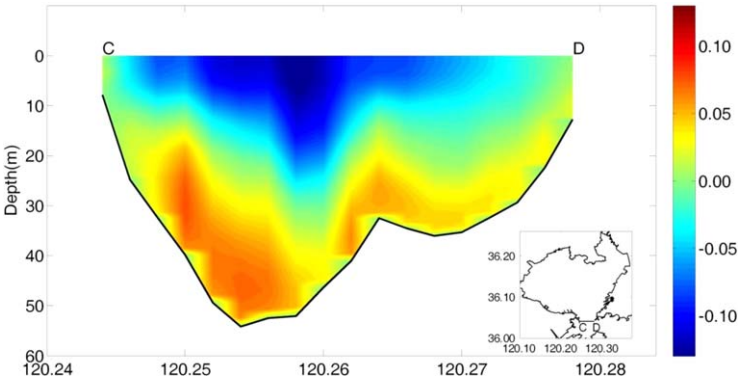

Figure 6. Vertical distribution of the tidally averaged density-driven current (m s^{-1}) over a cross section at the bay mouth. Positive current is defined to flow northward.

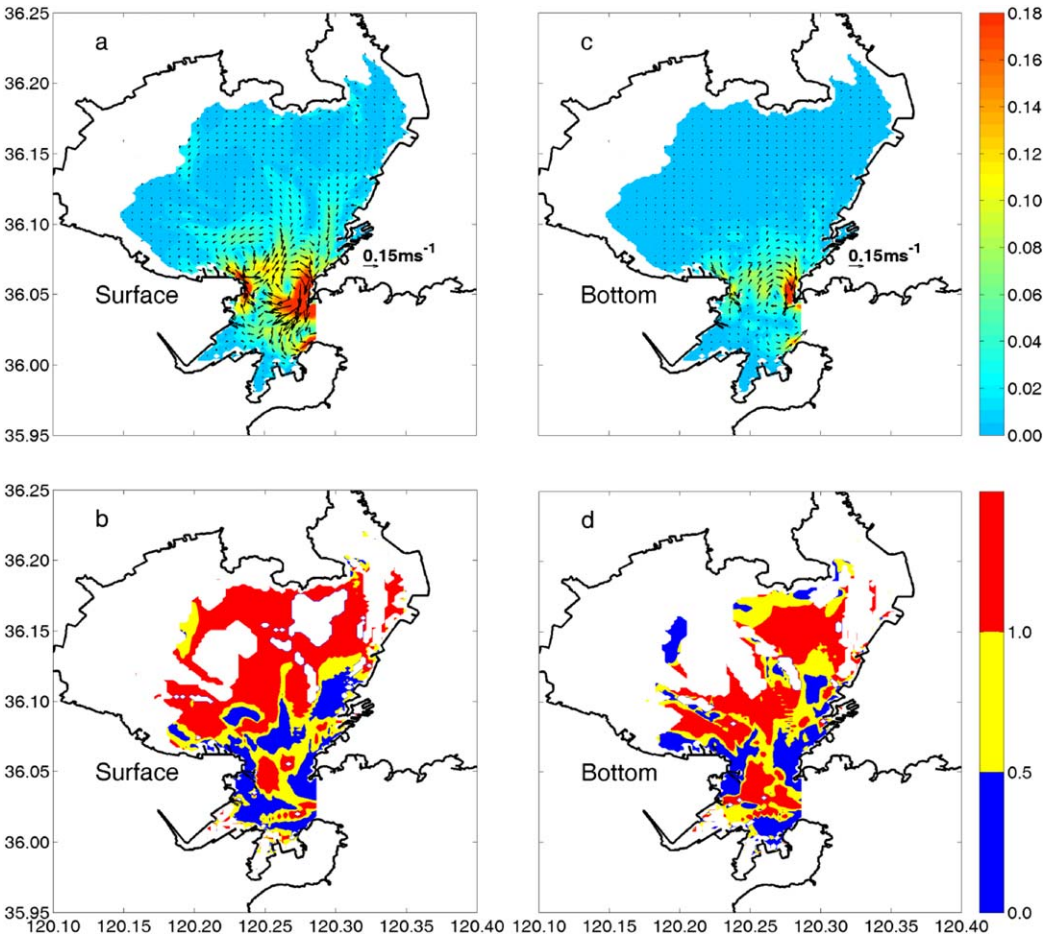

Figure 7. The tide-induced residual current in the (a) surface layer and (c) bottom layer, with color showing the magnitude of velocity; the ratio of magnitudes between the tidally averaged density-driven current and the tide-induced residual current in the (b) surface layer and (d) bottom layer.

data is sufficiently weak ($<$0.01 m s^{-1} in the surface layer and 0.005 m s^{-1} in the bottom layer), the relative difference was not calculated. According to Figures 9b and 9d, the vector difference between the two density-driven currents reaches $\sim$0.1 m s^{-1} at the bay mouth, and β_2 is close to or larger than 1.0 in some places (e.g., offshore of the Dagu River mouth and near the bay mouth) (Figures 9b and 9d). Therefore, the false current calculated with the nonsynchronous data is of the same order of magnitude as the density-driven current calculated with the synchronous data.

3.5. The Density-Driven Current Calculated With Tidally Averaged Synchronous Data

To examine the influence of climatological mean data on the calculation of the density-driven current, Case 3 was designed. In Case 3, the tidally averaged water temperature and salinity data are used for C^* in equation (1). The intratidal variations in the density field are not included in this calculation.

The density-driven current calculated with the tidally averaged synchronous data (Figures 10a and 10c) does not significantly differ from that calculated with the original hourly synchronous data (Figures 5a and 5b). The magnitude ratio β_2 (Figures 10b and 10d) is $<$0.5 in most areas of JZB. Generally, the magnitude of density-driven current calculated from tidally averaged data is slightly larger ($\sim$5%) than that by synchronous data.

4. Impact of Data Type on the Diagnostic Model

The results in section 3 indicate that the nonsynchronous data fail to accurately reproduce the density-driven current, whereas the tidally averaged data are capable of showing the basic pattern of the density-driven current. To

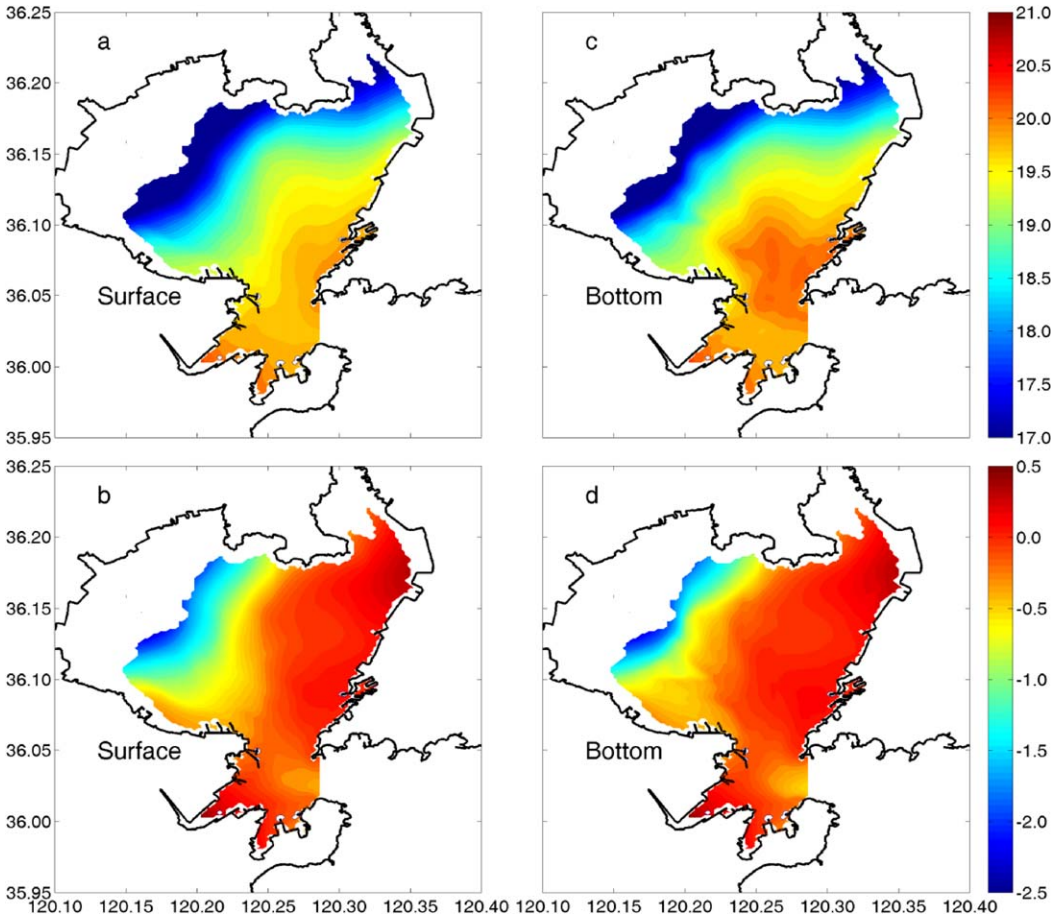

Figure 8. The density field (σ_t) in the (a) surface layer and (c) bottom layer and the density difference between the nonsynchronous data and the tidally averaged synchronous data in the (b) surface layer and (d) bottom layer. The nonsynchronous data were obtained by the virtual observation described in section 2.1.

understand the causes of these results, the horizontal pressure gradient and vertical turbulent viscosity (VTV) are analyzed here. These two variables are major factors influencing the modeled density-driven current.

4.1. Horizontal Pressure Gradient

To analyze the influence of the nonsynchronous data on the calculated baroclinic horizontal pressure gradient, we separated the driving force of the density-driven current into two components: a steady part and an oscillatory part. The steady part is defined as the tidal average of the pressure gradient, and the oscillatory part represents its intratidal variation.

The pressure gradient force at depth z_0 in the horizontal direction x can be decomposed into two terms:

$$\frac{\partial}{\partial x}\int_{z_0}^{\eta} g\rho dz = g\left(\int_{z_0}^{\eta}\frac{\partial \rho}{\partial x}dz + \rho_{z=\eta}\frac{\partial \eta}{\partial x}\right), \tag{6}$$

where ρ is the water density, g is the gravity acceleration (9.8 m s^{-2}), and η is the sea level. The density observed by the synchronous observations and the water level in the model can be assumed to be the sum of its tidally averaged value and intratidal part:

$$\begin{cases} \rho = \bar{\rho} + \rho' \\ \eta = \bar{\eta} + \eta' \end{cases}, \tag{7}$$

where $\bar{\rho}$ is tidally averaged density, $\bar{\eta}$ is the tidally averaged sea level, and ρ' and η' are their intratidal variations, respectively. For simplicity, we assume that $\rho' = a\cos(\omega t - \varphi_a)$ and $\eta' = b\cos(\omega t - \varphi_b)$, where a and b

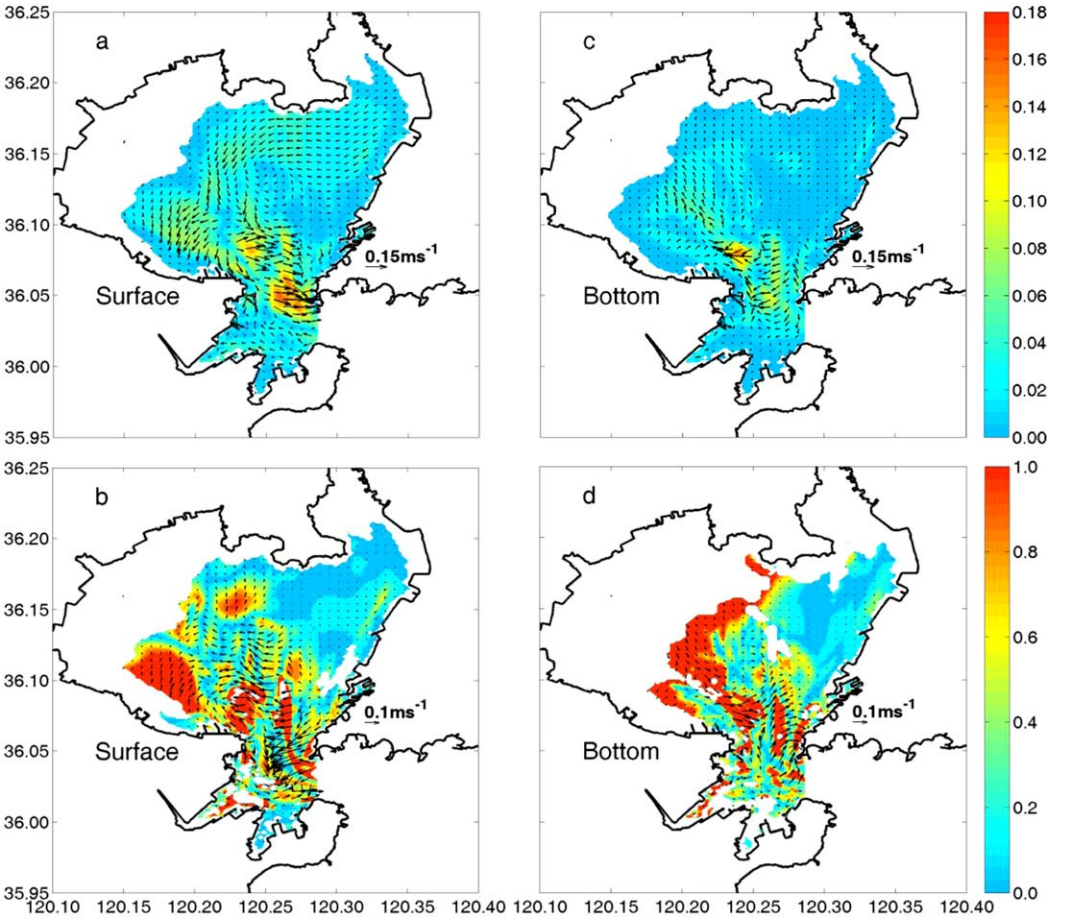

Figure 9. (a and c) The density-driven current calculated with the nonsynchronous data and (b and d) the difference in the density-driven current between Case 1 and Case 2, as defined by equation (5). Arrows show the vector difference and color shows the relative difference. (left) The results in the surface layer and (right) the results in the bottom layer.

are amplitudes, φ_a and φ_b are phases, and ω is frequency. These functions satisfy the conditions $\int_0^T \rho' dt = 0$ and $\int_0^T \eta' dt = 0$, where T is the tidal period.

The characteristic value of $\frac{\partial \rho}{\partial x}$ is $\frac{\Delta\overline{\text{rho}} + \Delta A}{L}$, where $\overline{\text{rho}}$, A, and L are the characteristic values of the tidally averaged density, the intratidal variation of density, and the horizontal scale, respectively, and Δ represents the spatial variation of a variable. The first term (the vertical integration of the horizontal density gradient) on the right side of equation (6) has a characteristic value of $\frac{gH(\Delta\overline{\text{rho}} + \Delta A)}{L}$, where H is the characteristic value of the water depth. In Case 3, the density-driven current was calculated using the tidally averaged density data. The term $\frac{gH\Delta A}{L}$ is zero when averaged over a tidal cycle.

During the nonsynchronous observation cruise (i.e., the virtual cruise), data at different stations were inevitably measured in different tidal phases. Hence, the intratidal variation in the density field results in an error of $\frac{gHA}{L}$ in $\frac{gH(\Delta\overline{\text{rho}} + \Delta A)}{L}$. The amplitude of the intratidal variation of density is considerable when compared with the horizontal mean density difference Δ rho. For instance, the virtual observation measures Station 17 at about high tide but Station 7 at about low tide (Table 1) and estimates a surface layer density difference between Station 17 and Station 7 of $\sim$3.4 kg m^{-3}. However, the tidally averaged observation data show a surface layer density difference of only $\sim$1.7 kg m^{-3} between the two stations. Hence, nonsynchronous observation can introduce significant errors in the density gradient. Although we conducted only one virtual cruise, such errors cannot be avoided for any nonsynchronous cruise in JZB because cruises usually last for 9–15 h, which is close to the M_2 tidal period in JZB, according to observations.

The modeled flow field driven by the tidally averaged temperature and salinity data in Case 3 was consistent with the tidally averaged flow field driven by the hourly synchronous data in Case 1. This consistency

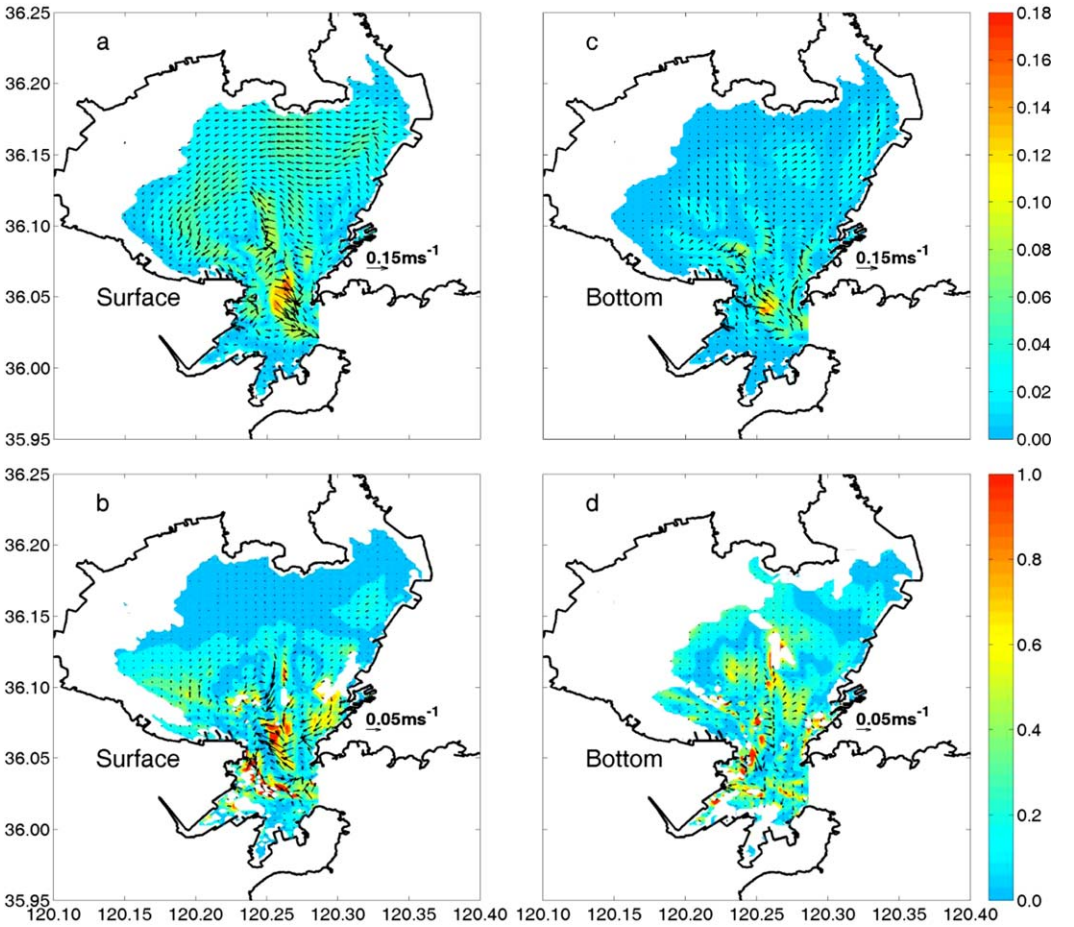

Figure 10. (a and c) The density-driven current calculated with tidally averaged data and (b and d) the difference in the density-driven current between Case 1 and Case 3 as defined by equation (5). Arrows show the vector difference and color shows the relative difference. (left) The results in the surface layer and (right) the results in the bottom layer.

implies that the impact of the intratidal variation in temperature and salinity fields on density-driven current is rather limited. The tidally averaged baroclinic horizontal pressure gradient can be obtained from equations (6) and (7):

$$\begin{aligned}\frac{1}{T}\int_0^T\left(\frac{\partial}{\partial x}\int_{z_0}^{\eta} g\rho dz\right)dt &= \frac{g}{T}\int_0^T\left(\frac{\partial}{\partial x}\int_{z_0}^{\bar{\eta}}\rho dz+\frac{\partial}{\partial x}\int_{\bar{\eta}}^{\eta}\rho dz\right)dt\\ &= \frac{g}{T}\int_0^T\left(\int_{z_0}^{\bar{\eta}}\frac{\partial\rho}{\partial x}dz+\rho_{z=\bar{\eta}}\frac{\partial\bar{\eta}}{\partial x}+\int_{\bar{\eta}}^{\eta}\frac{\partial\rho}{\partial x}dz+\frac{\partial\eta}{\partial x}\rho_{z=\eta}-\rho_{z=\bar{\eta}}\frac{\partial\bar{\eta}}{\partial x}\right)dt\\ &= g\int_{z_0}^{\bar{\eta}}\frac{\partial\bar{\rho}}{\partial x}dz+g\bar{\rho}_{z=\eta}\frac{\partial\bar{\eta}}{\partial x}+\frac{g}{T}\int_0^T\int_{\bar{\eta}}^{\eta}\frac{\partial\rho}{\partial x}dzdt+\frac{g}{T}\int_0^T\rho'_{z=\eta}\frac{\partial\eta'}{\partial x}dt.\end{aligned} \tag{8}$$

Clearly, the characteristic values of the parts of baroclinic horizontal gradient explained by the tidally averaged density (the first two terms on the right-hand side of the final equation) are $gH\Delta\overline{\text{rho}}/L$ and $g\overline{\text{rho}}\,\Delta\overline{\Gamma}/L$, and the parts explained by the intratidal variation of density (the last two terms) are $g\Gamma'\Delta\text{rho}/L$ and $gA\Delta\Gamma'/L$. Here $\overline{\Gamma}$ and Γ' are the characteristic values of the tidally averaged and intratidal variation of sea level, respectively. The ratios of the last two terms to the first term are $\Delta\text{rho}\,\Gamma'/\Delta\overline{\text{rho}}\,H$ and $A\Delta\Gamma'/\Delta\overline{\text{rho}}\,H$, respectively. In the calculations, Γ' (~1.5 m) and $\Delta\Gamma'$ (~0.1 m) are smaller than H (~10 m), $\Delta\overline{\text{rho}}$ and Δ rho are approximately the same size (<3 kg m^{-3}) and A (~1 kg m^{-3}) is smaller. Therefore, the intratidal variation of density cannot induce a significant difference in the average horizontal pressure gradient.

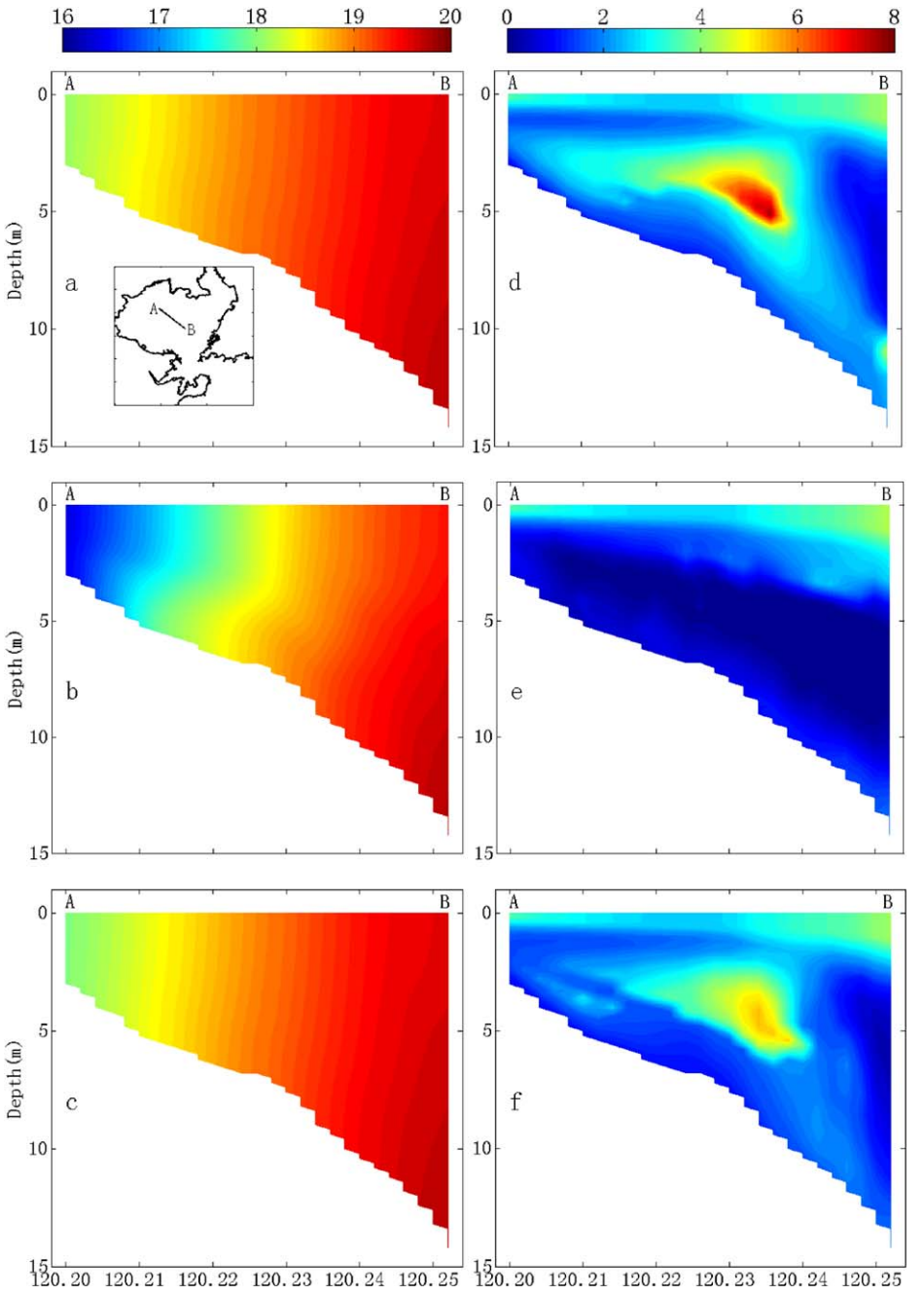

Figure 11. (a–c) The vertical structure of the modeled density (σ_t) and (d–f) the vertical turbulent viscosity ($m^2\ s^{-1}\cdot 10^{-3}$) in (a and d) Case 1 (synchronous data), (b and e) Case 2 (nonsynchronous data), and (c and f) Case 3 (tidally averaged data) in section AB off the Dagu River mouth (shown in Figure 11a). The density and vertical turbulent viscosity are averaged over a tidal cycle for simplicity.

4.2. Vertical Turbulent Viscosity

The interaction between the horizontal density gradient and the vertical current shear leads to a forcing mechanism known as "tidal straining" [*Simpson et al.*, 1990], which tends to produce periodic stratification. As described in section 3.4, the horizontal density gradient, especially off the Dagu River mouth, increases in the nonsynchronous data, which would lead to vertical stratification through tidal straining. Furthermore, the vertical stratification would affect the VTV [*Simpson*, 1997; *Simpson et al.*, 2005], and density-driven current would vary with the change in VTV. In this section, the modeled density and VTV in Cases 1 (synchronous data), 2 (nonsynchronous data), and 3 (tidally averaged data) in the section off the Dagu River mouth (shown in Figure 11a) are examined. These two variables are averaged over a tide cycle for simplicity. In

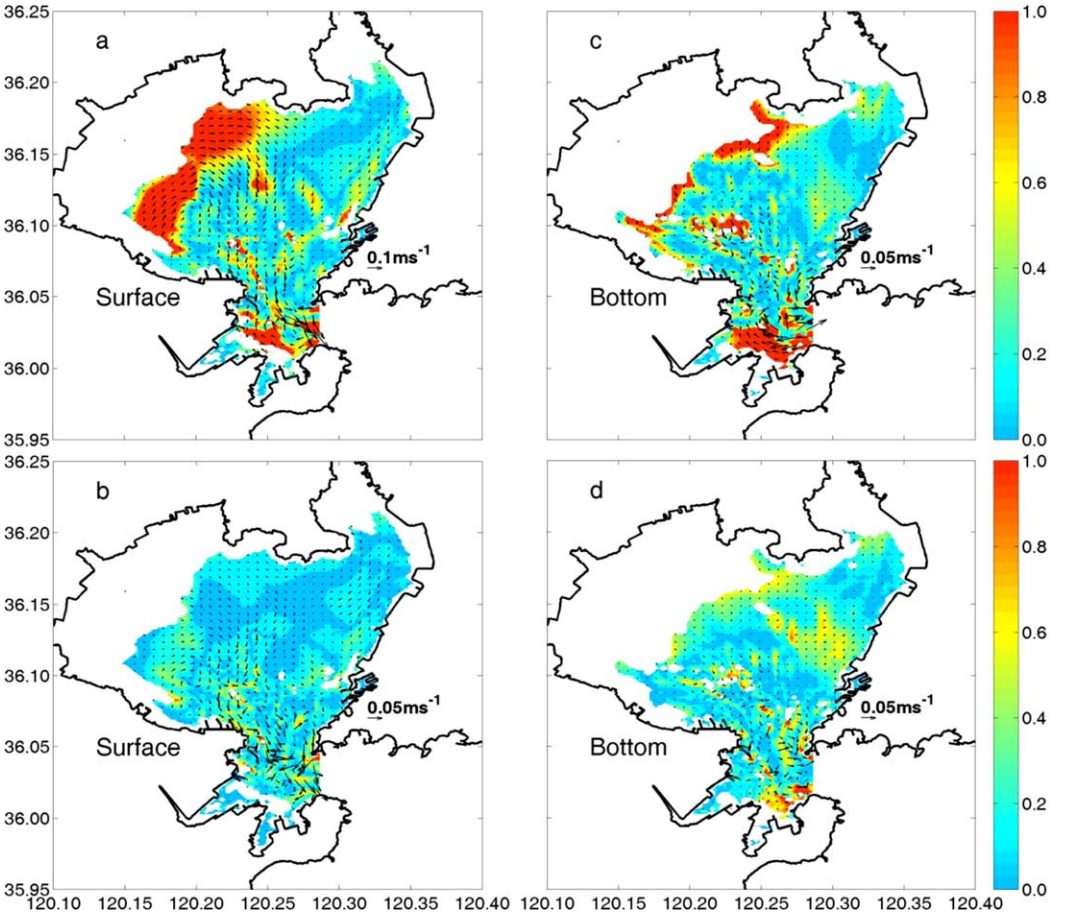

Figure 12. The difference in the density-driven current (a and c) between Case 1 and Case 4 and (b and d) between Case 1 and Case 5 as defined by equation (5). Arrows show the vector difference and color shows the relative difference. (left) The results in the surface layer and (right) the results in the bottom layer.

Cases 1 and 3, the density is almost homogenous in the vertical direction (Figures 11a and 11c), whereas stratification appears with the larger horizontal density gradient in Case 2 (Figure 11b). The VTV in Cases 1 and 3 has the same pattern, but the VTV in Case 2, especially in the lower layers, is quite different from that in Case 1.

It should be pointed out that vertical current shear would be different if different data types are used, which would affect the VTV in the model. However, more emphasis should be given to the influence of different VTV on the calculation of density-driven current than to the mechanism of the change in the VTV. Toward this end, two additional experiments, Cases 4 and 5, were conducted. In Case 4, the synchronous data and the VTV coefficient from Case 2 were used, whereas Case 5 used the synchronous data and the VTV coefficient from Case 3 (Table 2). The differences between these two cases and Case 1 were calculated according to equation (5). The primary difference between Case 1 and Case 4 is located around the Dagu River mouth, where the horizontal density gradient is large and the relative difference in density-driven current is greater than 1.0 (Figures 12a and 12c). Therefore, changes in both the horizontal density gradient and the vertical turbulent viscosity due to use of the nonsynchronous data influence the density-driven current. In contrast, the differences between Cases 1 and 5 are relatively small (Figures 12b and 12d), indicating that changes in the vertical turbulent viscosity that were introduced by the use of tidally averaged data have limited influence on the density-driven current.

From the above discussion on the impact of the data used in the model, some suggestions can be made for using observational data in the diagnostic model. First, calculations of the density-driven current using nonsynchronous data observed in a tidal-current-dominated area will be inaccurate. In JZB, if the observation

time is similar to or longer than a tidal period, it is impossible to obtain the basic pattern of density-driven current from a diagnostic model using nonsynchronous data. Second, the climatological mean data obtained by averaging observational data taken repeatedly at the same places are potentially useful in diagnostic models to obtain the density-driven current pattern. In JZB, the direction of density-driven current calculated from tidally averaged data is consistent with that from synchronous data, although the magnitude is slightly larger by about 5%. In practice, it is therefore necessary to examine whether the data averaging method may effectively eliminate intratidal variations in the density field.

5. Conclusions

Using a robust diagnostic model, the density-driven current was calculated using synchronous observational data in JZB. The density-driven current is characterized by a gravitational circulation, i.e., intrusion of high-density water in deep areas and outflow of low-density water in shallow areas. The current calculated in the diagnostic model depends strongly on the type of observational data used in the model. In areas such as JZB, where the intratidal variation in the density field is significant and comparable to the spatial variation in the density field, nonsynchronous data will inevitably induce considerable errors in the calculated density-driven current. In a nonsynchronous survey, the data taken at different stations will generally not be measured in the same tide phases; these intratidal variations will introduce errors in the density gradient and vertical turbulent viscosity. However, using the tidally averaged density field obtained by averaging the synchronous data did not induce significant errors into the calculated density-driven current. The findings in this study will help to design more suitable observation plans in tide-dominated water bodies like JZB.

Acknowledgments
The study was financially supported by the Special Fund for Public Welfare Industry (Oceanography) (grant 200805011). The authors would like to thank all the crews involved in the survey and Guangliang Liu, Jing Xu, Jiuzhi Yan, and Jian Zhao for their assistance in data processing. We are also grateful to the High Performance Center of Ocean University of China for their technical support for our programs running on the computing cluster.

References

Blumberg, A. F., and G. L. Mellor (1987), A description of a three-dimensional coastal ocean circulation model, in *Three-Dimensional Coastal Ocean Models, Coastal Estuarine Sci.*, vol. 4, edited by N. S. Heaps, pp. 1–16, AGU, Washington, D. C., doi:10.1029/CO004p0001.

Chen, C. S., R. B. Ji, L. Y. Zheng, M. Y. Zhu, and M. Rawson (1999), Influences of physical processes on the ecosystem in Jiaozhou Bay: A coupled physical and biological model experiment, *J. Geophys. Res.*, *104*(C12), 29,925–29,949, doi:10.1029/1999JC900203.

Chen, D. X., X. P. Sun, and Y. X. Pu (1992), *Marine Atlas of Bohai Sea, Yellow Sea, East China Sea: Hydrology* [in Chinese], China Ocean Press, Beijing.

Chen, J. R., X. E. Chen, M. H. Yu, Y. W. Yan, S. L. Shan, and J. Zhao (2011), Three-dimensional high-resolution numerical study of the tide and tidal current in the Jiaozhou Bay [in Chinese with English abstract], *Period. Ocean Univ. China*, *41*(7), 29–35, doi:10.3969/j.issn.1672–5174.2011.07.005.

Ding, W. L. (1992), Tide and tidal current [in Chinese], in *Ecology and Living Resources of Jiaozhou Bay*, edited by R. Y. Liu, pp. 39–72, Science, Beijing.

Fujio, S., and N. Imasato (1991), Diagnostic calculation for circulation and water mass movement in the deep Pacific, *J. Geophys. Res.*, *96*(C1), 759–774, doi:10.1029/90JC02130.

Guo, X. Y., and T. Yanagi (1996), Seasonal variation of residual current in Tokyo Bay, Japan-diagnostic numerical experiments, *J. Oceanogr.*, *52*(5), 597–616, doi:10.1007/BF02238323.

Guo, X. Y., A. Futamura, and H. Takeoka (2004), Residual currents in a semi-enclosed bay of the Seto Inland Sea, Japan, *J. Geophys. Res.*, *109*, C12008, doi:10.1029/2003JC002203.

Han, S. Z., J. Zhao, F. B. Wei, and J. Lin (2007), 3D Numerical simulation of the fresh water and sediment in the Dagu estuary of Jiaozhou Bay during the flood season [in Chinese with English abstract], *Period. Ocean Univ. China*, *37*(5), 689–694.

Holland, W. R., and A. D. Hirschman (1972), A numerical calculation of the circulation in the North Atlantic Ocean, *J. Phys. Oceanogr.*, *2*(4), 336–354, doi:10.1175/1520-0485(1972)002<0336:ANCOTC>2.0.CO;2.

Lee, H. J., and S. Y. Chao (2003), A climatological description of circulation in and around the East China Sea, *Deep Sea Res., Part II*, *50*(6), 1065–1084, doi:10.1016/S0967-0645(03)00010-9.

Lee, H. J., S. Y. Chao, and K. Liu (2004), Effects of reduced Yangtze River discharge on the circulation of surrounding seas, *Terr. Atmos. Ocean Sci.*, *15*(2), 111–132.

Liu, K. K., S. Y. Chao, H. J. Lee, G. C. Gong, and Y. C. Teng (2010), Seasonal variation of primary productivity in the East China Sea: A numerical study based on coupled physical-biogeochemical model, *Deep Sea Res., Part II*, *57*(19), 1762–1782, doi:10.1016/j.dsr2.2010.04.003.

Liu, S. M., J. Zhang, H. T. Chen, and G. S. Zhang (2005), Factors influencing nutrient dynamics in the eutrophic Jiaozhou Bay, North China, *Prog. Oceanogr.*, *66*(1), 66–85, doi:10.1016/j.pocean.2005.03.009.

Liu, Z., H. Wei, G. Liu, and J. Zhang (2004), Simulation of water exchange in Jiaozhou Bay by average residence time approach, *Estuarine Coastal Shelf Sci.*, *61*(1), 25–35, doi:10.1016/j.ecss.2004.04.009.

Liu, Z., H. Wei, J. Bai, J. Zhang, D. Liu, and S. Liu (2007), Nutrients seasonal variation and budget in Jiaozhou Bay, China: A 3-dimensional physical–biological coupled model study, *Water Air Soil Pollut.*, *7*(6), 607–623, doi:10.1007/s11267-007-9128-8.

Lou, A. G., Y. B. Hu, L. Kuang, X. Q. Zhang, and P. Du (2009), Analysis and prediction of influence imposed on Jiaozhou Bay tidal currents and tidal energy of M_2 tidal system by Jiaozhou Bay reclamation, *J. Ocean Univ. China*, *8*(1), 23–29, doi:10.1007/s11802-009-0023-y.

Lv, X. G., C. Zhao, C. S. Xia, and F. L. Qiao (2010), Numerical study of water exchange in the Jiaozhou Bay and the tidal residual currents near the bay mouth [in Chinese with English abstract], *Acta Oceanol. Sin.*, *32*(2), 20–30.

Mellor, G. L. (2004), Users guide for a three dimensional, primitive equation, numerical ocean model, report, 56 pp., Program in Atmos. and Oceanic Sci., Princeton Univ., Princeton, N. J.

Oey, L. (2005), A wetting and drying scheme for POM, *Ocean Modell.*, *9*(2), 133–150, doi:10.1016/j.ocemod.2004.06.002.
Sarkisyan, A. S., and V. F. Ivanov (1971), The combined effect of baroclinicity and bottom relief as an important factor in the dynamics of ocean current, *Izv. Acad. Sci. USSR Atmos. Oceanic Phys., Engl. Transl.*, *1*, 173–188.
Sarmiento, J. L., and K. Bryan (1982), An ocean transport model for the North Atlantic, *J. Geophys. Res.*, *87*(C1), 394–408, doi:10.1029/JC087iC01p00394.
Shi, J., G. Li, and P. Wang (2011), Anthropogenic influences on the tidal prism and water exchanges in Jiaozhou Bay, Qingdao, China, *J. Coastal Res.*, *27*(1), 57–72, doi:10.2112/JCOASTRES-D-09–00011.1.
Simpson, J. H. (1997), Physical processes in the ROFI regime, *J. Mar. Syst.*, *12*(1), 3–15, doi:10.1016/S0924–7963(96)00085-1.
Simpson, J. H., J. Brown, J. Matthews, and G. Allen (1990), Tidal straining, density currents, and stirring in the control of estuarine stratification, *Estuaries*, *13*(2), 125–132, doi:10.2307/1351581.
Simpson, J. H., E. Williams, L. H. Brasseur, and J. M. Brubaker (2005), The impact of tidal straining on the cycle of turbulence in a partially stratified estuary, *Cont. Shelf Res.*, *25*(1), 51–64, doi:10.1016/j.csr.2004.08.003.
Stewart, R. H. (2008), *Introduction to Physical Oceanography*, Dep. of Oceanogr., Texas A&M Univ., Tex.
Wang, C., X. Q. Zhang, and Y. L. Sun (2009), Numerical simulation of water exchange characteristics of the Jiaozhou Bay based on a three-dimensional Lagrangian model, *China Ocean Eng.*, *23*, 277–290.
Wright, D. G., K. R. Thompson, and Y. Lu (2006), Assimilating long-term hydrographic information into an eddy-permitting model of the North Atlantic, *J. Geophys. Res.*, *111*, C09022, doi:10.1029/2005JC003200.
Yanagi, T., and S. Takahashi (1993), Seasonal variation of circulations in the East China Sea and the Yellow Sea, *J. Oceanogr.*, *49*(5), 503–520, doi:10.1007/BF02237458.